JACS
JOURNAL OF THE AMERICAN CHEMICAL SOCIETY

Article

pubs.acs.org/JACS

A Polyoxometalate Cluster Paradigm with Self-Adaptive Electronic Structure for Acidity/Reducibility-Specific Photothermal Conversion

Chen Zhang,[†] Wenbo Bu,[*,†,§] Dalong Ni,[†] Changjing Zuo,[‡] Chao Cheng,[‡] Qing Li,[†] Linlin Zhang,[†] Zheng Wang,[†] and Jianlin Shi[*,†]

[†]State Key Laboratory of High Performance Ceramics and Superfine Microstructure, Shanghai Institute of Ceramics, Chinese Academy of Sciences, Shanghai 200050, P.R. China

[§]Shanghai Key Laboratory of Green Chemistry and Chemical Processes, School of Chemistry and Molecular Engineering, East China Normal University, Shanghai 200062, P.R. China

[‡]Department of Nuclear Medicine, Changhai Hospital, Shanghai 200433, P.R. China

Supporting Information

ABSTRACT: Photothermal conversion is one of the most important keys in the fields of solar collection, photo-hyperthermia, etc., and its performance is highly dependent on the photothermal conversion materials used. Especially in cancer photo-hyperthermia, the presently available small-molecule- or nanomaterial-based agents still suffer from numerous drawbacks, such as nonspecific accumulation and inevitable side effects on normal tissues. Here we identify a Mo-based polyoxometalate cluster that can change its dimension from small (1 nm) to big (tens of nanometer), favoring its intratumoral accumulation, and enhance photothermal conversion in response to the intratumoral acidity and reducibility, demonstrating a previously unrealized tumor-specific photo-hyperthermia. Distinct from the well-researched nano-based agents, a unique electronic structure of this cluster has been identified as the origin of the observed acidity-induced self-assembly and reduction-promoted NIR absorbance. In addition to providing a promising clinical agent, this finding is expected to establish a new physicochemical paradigm for photothermal materials design based on clusters.

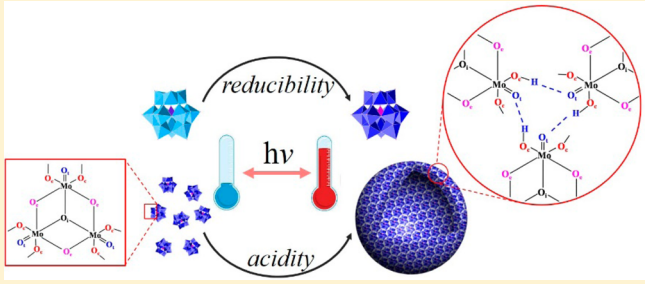

1. INTRODUCTION

The concept of photothermal conversion has attracted great attention over the past decade, with potential applications in various fields such as solar collection,[1] photothermal catalysis,[2] microcontrollers,[3] and especially photo-hyperthermia for cancer treatment.[4] In spite of being recognized as an efficient and hypoxic-independent technology in advanced cancer therapy,[4−6] nanomaterials-mediated photo-hyperthermia still faces great challenges in clinical translation. Those reported high-performance photothermal nano-agents mainly involve various plasmonic metals,[7,8] compounds composed of transition metals and oxygen group elements,[9−12] carbon species,[13−16] and organic conjugated polymers.[17−20] However, besides the pursuit of enhanced therapeutic efficiency and safety, the search for satisfactory therapeutic nano-agents is not a simple medical consideration; numerous multifaceted requirements on a clinical agent, including low cost, volume production, storability, and so on, continue to retard the progress of these laboratorial samples toward nosocomial agents.

A common concern about the cancer photothermal therapy is the reduced therapeutic efficiency and the unknown long-term biological consequences of the photothermal nano-agents embedded in normal tissues due to the nonspecific uptake of the agents. In addition, it is possible that off-target heating may induce mis-hyperthermia on these noncancerous regions that are immediately adjacent to the irradiated tumor, which makes side effects unavoidable on normal tissues. Technically, one available strategy is to improve the accumulation of photothermal agent in tumors through active targeting modification.[21] Unfortunately, the current targeted accumulation efficiencies are still far from being satisfactory, and consequentially new concerns arise from the complicated synthetic process and the chemical or biostability of these sensitive targeting groups.[21−23] Moreover, a dilemma presents in the nano-agent design for promoting the passive accumulation approaches, which depend mainly on the prolonged systemic circulation and efficient enhanced permeability and retention (EPR) effect. Generally, nanoparticles of small size (<10 nm) more easily escape via rapid removal by mononuclear phagocyte systems with relatively long circulation, but show poor EPR effect in the effective delivery into cancer tissues, and the case is exactly the opposite for those larger ones.[24,25] For addressing the intractable dilemma, besides the available "big-

Received: April 1, 2016
Published: June 6, 2016

DOI: 10.1021/jacs.6b03375
J. Am. Chem. Soc. 2016, 138, 8156−8164

small" approach to transforming microstructures to nanostructures in situ to bypass EPR,[26] an alternate strategy is to design a "small-big" photothermal agent, which could stay small-molecule-like during circulation in the bloodstream and then self-assemble to big molecules in tumors under activation by the tumor microenvironment.[27]

On the other hand, addressing the inevitable capture of the nano-agents by nontumorous regions and the consequent mis-hyperthermia therein, a feasible approach to prevent possible side effects is to differentiate the photothermal conversion efficiency between the agents inside and outside the tumor, namely to realize a self-adaptive conversion mechanism, which features sensitive and specific responses to the tumors' physicochemical characteristics. From a physical point of view, the photothermal effect essentially depends on the resonant oscillation of delocalized electrons under an external electromagnetic field.[28] All these considerations stimulate the chemical community to search for qualified photothermal conversion nanomaterials with sensitive electronic structure to achieve tumor-specific hyperthermia.

Here, we report a Mo-based polyoxometalate (POM) cluster as the desirable near-infrared (NIR) photothermal agent that benefits from a high tissue penetration depth.[29] These extremely soluble POMs, obtained from a fast, large-scale synthesis, are highly stable and storable, even in a high ionic strength medium (Figures S1 and S2). Tailored to the tumor microenvironment featuring both mild acidity and reducibility,[30,31] the low-pH-induced self-assembly and self-adaptive photothermal conversion of this distinct cluster have been found and investigated from microcosmic mechanism to *in vivo* administration, representing a smart cluster-based photothermal agent for tumor-specific therapy with significant clinical prospects.

2. RESULTS AND DISCUSSION

2.1. Low-pH-Induced Self-Assembly. The synthesized POM powders are ionic compounds composed of cations (Na^+ and NH_4^+) and Keggin-type macroanionic units which have highly hydrophilic surfaces to render them extremely soluble (Table S1). As the transmission electron microscopic (TEM) image shows (Figure 1a), these clusters are highly uniform with

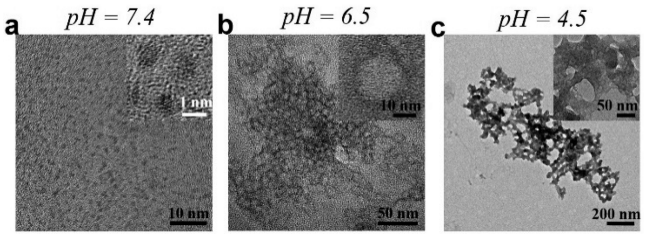

Figure 1. TEM images of the POM clusters at pH = 7.4 (a), self-assembled nanovesicle at pH = 6.5 (b), and the much larger assemblies at pH = 4.5 (c). Insets in the upper right corners are the corresponding zoom-in images.

an ultrasmall diameter of ca. 1 nm in pH = 7.4 dispersion medium, corresponding to a stable hydrodynamic size of 1.7 nm observed in the time-course dynamic light scattering (DLS, Figure 2a) measurement. In addition, the observed lattice fringes in high resolution TEM (HRTEM) images indicate these clusters are crystalline with a well-defined microstructure. Very interestingly, in the subsequent acidification process, DLS

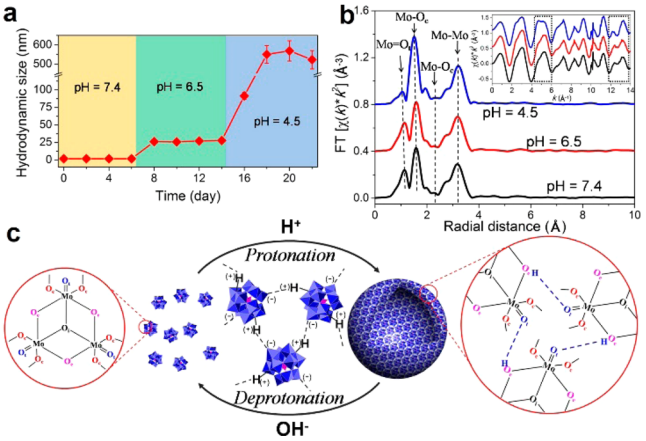

Figure 2. (a) DLS measurements monitoring the evolution of POM size in the solution with successive acidifications from pH = 7.4 to 6.5 and to 4.5 (n = 3, mean ± s.d). (b) Fourier-transformed spectra of the k^2-weighted Mo K-edge EXAFS oscillations for the POM clusters dispersed in solutions of different pH values. Inset is the corresponding k^2-weighted oscillator functions. (c) Schematic diagram proposed for the low-pH-induced self-assembly of numerous POM cluster units into large hollow aggregate structure through protonation-induced hydrogen bonding.

measurement reveals these cluster blocks could self-assemble into larger but monodisperse assemblies with a diameter of ~25 nm in the mild acidity (Figure 1b). These collapsed nanovesicles during the drying process observed in TEM image show a high contrast around the edges, which confirms a hollow, lipid vesicle-like sphere formation and also suggests the non-covalent linkage among these POM blocks.[32,33] In addition, these stable large spherical assemblies could further aggregate into higher structured morphology in the medium through further acidification (pH = 4.5, Figures 1c and 2a) and remain hydrophilic, with an average hydrodynamic diameter of ~0.5 μm.

Subsequently, to gain fundamental insight into the low pH-triggered self-assembling behavior of these POM clusters, their extended X-ray absorption fine structure (EXAFS) was measured to reveal the microstructural changes. Fourier-transformed spectra of the k^2-weighted Mo K-edge oscillations (pair distribution function) for POM dispersed in the media of varied pH values are shown in Figure 2b. Noticeably, the limited scattering peaks with the absence of any high-order correlations confirm the cluster nature of the as-synthesized POM. During the successive acidification, the Mo═O_t (terminal oxygen) bond length in POM is slightly decreased with a lowered coordination number of terminal oxygen, in contrast to the also slightly reduced Mo−O_e (edge-sharing oxygen) distance but with an increased coordination number of edge-sharing oxygen. In addition, the bond distance for Mo−Mo and the corresponding coordination number remain unchanged. According to the previous speculation on the assembly of POM, the driving force of self-assembly can be attributed to a delicate balance between short-range attractive forces and electrostatic repulsions between adjacent anion clusters.[32] These results substantiate the theoretical inference of protonation on the edge-sharing oxygen atoms and subsequent hydrogen bonding between O_e or O_t and the proton once acidified.[34] Understandably, in the medium of pH = 7.4, these POM macroanions are well-ionized with high charge density to repulse each other, which renders them extremely stable in

DOI: 10.1021/jacs.6b03375
J. Am. Chem. Soc. 2016, 138, 8156−8164

small clusters. However, the acidification-induced protonation of POM macroanions will significantly decrease the electrostatic repulsions with the decreasing charge density and, simultaneously, increase the attractive forces through the hydrogen bond formation. The subsequent re-balance between these opposite interactions results in the self-assembly behavior of POM at lowered pH, whose assembly degree correspondingly changes with the change of pH value (Figure 2c).

2.2. Self-Adaptive Photothermal Conversion Sensing Surrounding Acidity and Reducibility. Interestingly, we found that the low-pH-induced self-assembly of POM led to an enhanced absorption peak and its significant blue-shift to 808 nm (Figures 3a and S3), which corresponds to one of the most

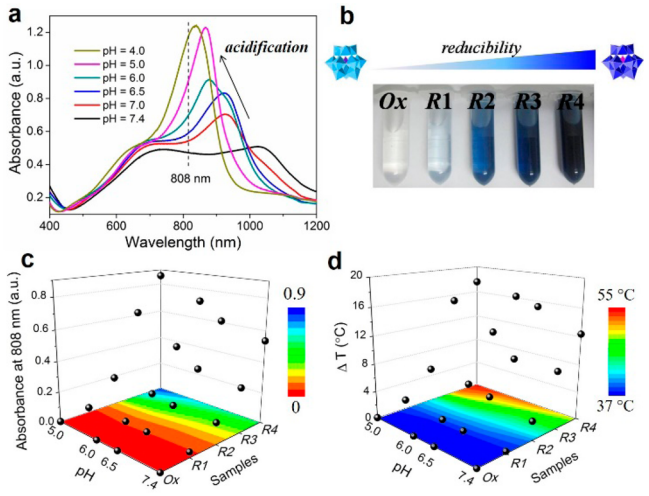

Figure 3. (a) UV−vis absorptions of POM nanocluster solutions (100 ppm Mo) at varied pH values. (b) Digital photographs of POM cluster aqueous solutions under successive reductions. Acidity- and reducibility-dependent absorbances at 808 nm (c) of POM cluster solutions (100 ppm Mo) and their corresponding temperature increases (d) under the irradiation of an 808 nm NIR laser at a power density of 1.5 W cm^{-2} for 5 min.

commonly available NIR lasers in clinics, with high penetration depth. In addition, the blue color of POM solution deepens monotonically in the successive reductions, corresponding to a proportionally increasing NIR absorbance (Figures 3b and S4). Subsequently, the acidity- and reducibility-dependent absorbance at 808 nm results in a wide-range adjustable photothermal conversion, such that a more efficient temperature rise under 808 nm laser irradiation can be obtained at lower pH values and, more prominently, at stronger reductions (Figure 3c,d).

To reveal the underline mechanism of such a unique photothermal conversion of POM clusters, their electron system and structural characteristics were further investigated. The cyclic voltammogram of POM shows three pairs of reversible oxidation/reduction peaks at a fast sweep rate (Figure 4a), indicating a flexibly reversible multi-electron process without the cluster decomposition according to the surrounding variation. X-ray photoelectron spectroscopy (XPS) indicates that part of the molybdenum in POM is reduced from VI to V oxidation state in the multi-electron reduction process, endowing these reduced POM clusters with mixed-valence states (Figure 4b). Furthermore, as the electron spin resonance (ESR) spectroscopic results show, in addition to the observed Mo(V) signal at the g value of 1.92, there is another weak line at the g value of free electron (g = 2.0023) in these reduced POM (Figure 4c), confirming the existence of mobile electrons in the cluster framework. Additionally, the significantly enhanced peaks of Mo−O_e (ca. 1.9 Å) and Mo−Mo (ca. 3.2 Å) bonds observed in the RDF accompanying the increasing reduction level in POM indicate that these mobile electrons are delocalized over the mixed-valence Mo sites in the trimetallic group [Mo_3O_{13}] (Figure 4d).

In the POM structure, the lowest unoccupied molecular orbital (LUMO) is mainly localized on the Mo atoms, and the highest occupied molecular orbital (HOMO) is mainly localized on the bridging oxygen atoms (O_c and O_e).[35,36] The fact of the charge transfer between Mo(V) and Mo(VI) through the bridging oxygen bonds in POM is known to be the origin of the typical NIR absorption of POM,[37] leading to their NIR photothermal conversion behavior. Unlike those conventional nano-based photothermal agents, whose photothermal effects are mainly dependent on their surface or internal resonant oscillation of conduction electrons, the entirely naked electronic structure in the POM cluster is sensitive to the pH and reductive environment in the aqueous surroundings. Briefly, the acidity broadens the HOMO−LUMO gap via the protonation of the edge-sharing oxygen atoms, resulting in a closer NIR absorption peak to 808 nm. The intensified reduction of the clusters will promote the delocalized electron density and occupiable cation site (Mo(V)) through the reversible multi-step electron exchange, which, in the meantime, will simultaneously strengthen the electron relaxation polarization under the external electromagnetic field (light). The revealed reduction-enhanced dielectric constant of POM confirms the more efficient electron relaxation polarization in the deeper-reduced state, indicating an improved exothermic polarization loss to consume and convert the light energy (Figure 4e,f). As a result, the NIR absorption and subsequent photothermal conversion efficiency are largely enhanced. All these unique characteristics enable the POM clusters to be a both acidity and reducibility dual-sensitive self-adaptive photothermal agent.

2.3. Clearance and Biodistribution. The pharmacokinetics of the injectable nanomaterial-based agents is often a major concern for their clinical translations, so the blood circulation behavior of POM was then investigated. The time-dependent concentration change of Mo in the blood indicates a classical two-component pharmacokinetic model with the terminal elimination half-lives of 25 min and 9.9 h for the central component and peripheral component, respectively (Figure 5a). The subsequent Mo content analysis in excretion reveals their continuous decrease from a high concentration in urinary, corresponding to an accumulative urinary clearance up to 73% injected dose (ID) in a week after injection (Figures 5b and S5). This fast clearance suggests the rapid renal filtration and urinary excretion from the body, which is believed to benefit from their extremely small hydrodynamic diameter of 1.7 nm in the neutral medium and outstanding hydrophilicity.[25,38] In contrast, the Mo concentration in feces is relatively low and reaches peak level on the second day post injection. The accumulative clearance of POM by feces reaches a stable 18% ID in a week, indicating other clearance route through liver metabolism. Notably, most of the injected POM can be excreted in a week (considering the unavoidable loss of the agent in the excretion−collection process, more than 91% ID are excreted), this small-molecule-like fast excretion clearance from the body could circumvent potential long-term toxicity *in vivo*.

DOI: 10.1021/jacs.6b03375
J. Am. Chem. Soc. 2016, 138, 8156−8164

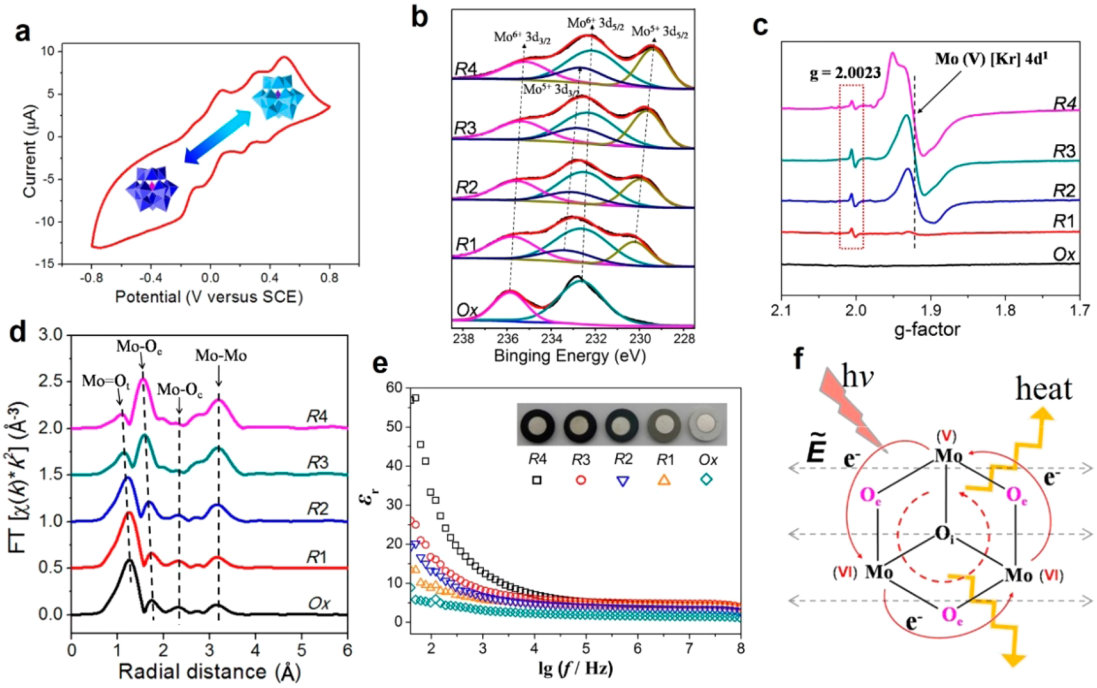

Figure 4. (a) Cyclic voltammogram obtained from POM-adsorbed GC electrodes measured in 0.1 M H_2SO_4 solution. (b) XPS spectra of Mo 3d for POM clusters under successive reduction steps. (c) ESR spectra recorded at room temperature in X band for POM cluster powders. (d) Fourier transformed spectra of the k^2-weighted Mo K-edge EXAFS oscillations for the POM clusters dispersed in water under successive reduction steps. (e) Frequency-dependent dielectric constant of POM clusters at varied reduction levels measured at room temperature. (f) Schematic of photothermal conversion in the reductive POM cluster.

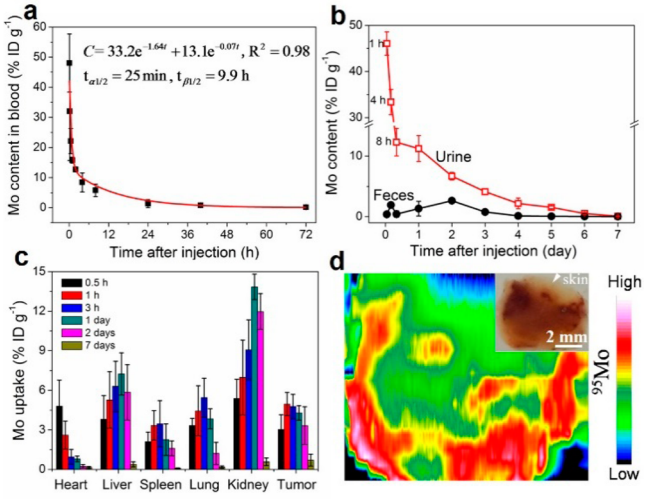

Figure 5. (a) Time-dependent concentrations of Mo in the blood. (b) Time-dependent concentrations of Mo in urine and feces (n = 3, mean ± s.d.). (c) Biodistribution of Mo in 4T1-tumor-bearing mice in 0.5 h, 1 h, 3 h, 1day, 2 days, and 7 days post injection (n = 3, mean ± s.d.). (d) Laser desorption/ionization mass spectrometry ^{95}Mo-mapping image of the largest-sectioned 4T1 tumor collected in 1 h post injection of POM. Inset is the corresponding digital photograph.

To assess the effectiveness of POM delivery, its biodistribution in normal organs and 4T1 xenografted tumor was examined (Figure 5c). Predictably, the intravenously (i.v.) injected POM exhibits rapid accumulations within 0.5 h and efficient clearances within a week in/from the main organs and tumor, due to the short two-component related terminal elimination half-life. The time period of the highest accumulation of POM in the tumor is in about 1 h post injection, corresponding to a high accumulation (5.1% injected dose per gram of organ, % ID g^{-1}), which is roughly commensurate with those in the liver and kidney in the same period. This significant intratumoral accumulation without any targeting modification is believed to result from the unique "small-to-big" self-assembly behavior from the isolated POM clusters in neutral environment before intratumoral accumulation to much larger ones in the acidic tumor microenvironment, which in the meantime facilitates the EPR effect, especially the retention effect once accumulated in the tumor. This hypothesis can be evidently confirmed by the much lower POM's clearance rate in the tumor than that in the heart without reticuloendothelial system (Figure S6). Then, the laser desorption/ionization mass spectrometry (LDIMS) was used to study the intratumoral microdistribution of POM (Figure 5d). In spite of the high intratumoral interstitial fluid pressure,[39,40] these clusters are distributed throughout the whole tumor region in 1 h post injection, suggesting their significant extravasation. The selective intratumoral accumulation and deep tumor penetration of POM within a short time period are the most essential prerequisites for subsequent efficient therapeutics.

2.4. Theranostic Effect Assessments. Before further photothermal therapy administration, the biosafety of these as-prepared POM clusters was primarily evaluated, presenting no detectable cytotoxicity *in vitro* and no significant side effects *in vivo*, even at high concentrations (Figures S7–S9). Their excellent biocompatibility is believed to benefit from the stable cluster structure without any decomposition and rapid excretion clearance. After the direct addition of POM without any further incubation, the subsequent POM-mediated photothermal therapy *in vitro* under 808 nm NIR laser irradiation shows a significant anticancer effect in contrast to the

DOI: 10.1021/jacs.6b03375
J. Am. Chem. Soc. 2016, 138, 8156–8164

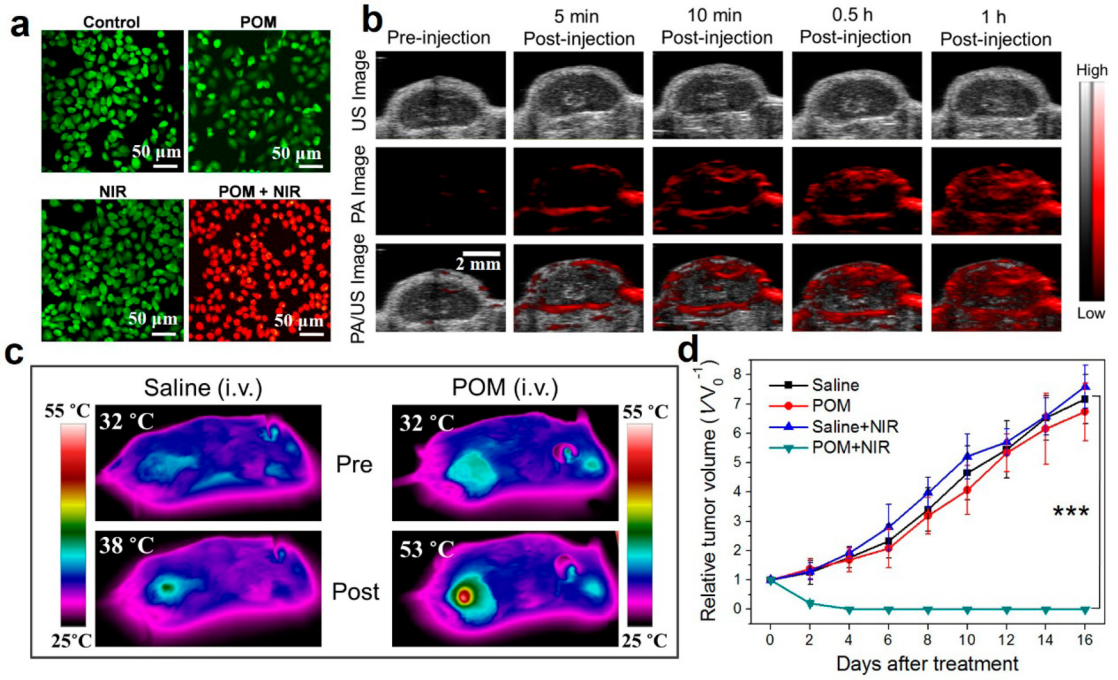

Figure 6. (a) Confocal images of propidium iodide and calcein-AM double-stained MCF-7 cells in different treatment groups containing Control, POM incubation (25 μg mL^{-1} Mo), NIR laser irradiation (1.5 W cm^{-2}, 5 min), and POM incubation + NIR laser irradiation. (b) Representative PA images and ultrasound images of a subcutaneous 4T1 tumor on a living mouse obtained before injection and in 5 min, 10 min, 0.5 h, and 1 h post i.v. injection of POM (30 mg Mo kg^{-1}). (c) Representative thermal response in 4T1 tumor-bearing mice in 1 h after intravenous injection before with saline or POM (30 mg Mo kg^{-1}). Thermal images were obtained respectively before and within 5 min of 808 nm laser irradiation (1.5 W cm^{-2}). (d) Relative tumor volumes in the 4T1 tumor-bearing mice received four different treatments of saline (i.v. injection), POM (30 mg Mo kg^{-1}, i.v. injection), saline + NIR (1.5 W cm^{-2} for 5 min), and POM + NIR (1.5 W cm^{-2} for 5 min, n = 5, mean ± s.d., ***P < 0.001).

undetectable influences on the groups treated with POM or NIR only (Figures S10 and 6a), the therapeutic efficiency is proportional to the concentration of POM and the power density of the laser.

The fast-decreased tumor within 30 min observed in the time-dependent photoacoustic (PA) imaging images indicates POM's potential to serve as an outstanding PA contrast agent, and further confirms the fact that POM exhibits efficient accumulation in tumor and could penetrate throughout the whole tumor region in 1 h post injection (Figures 6b and S11). Accordingly, these 4T1 tumor-xenografted mice were injected intravenously with POM (30 mg Mo kg^{-1}) or a saline control 1 h before NIR administration. Under the subsequent 808 nm laser irradiation, the tumor temperature in the POM-treated group rapidly reached 50 °C within 2 min and maintained at about 52 °C, whereas the tumors in mice injected with saline were limitedly heated to lower than 40 °C (Figures 6c and S12). Following the treatments, the tumors received POM injection or laser irradiation only grew rapidly, comparable to that in control group (saline treatment alone) over 16 days (Figure 6d). In contrast, the tumors in the POM-mediated photothermal treatment group were efficiently inhibited, corresponding to the complete tumor ablation in 4 days without any relapse and later lung metastasis until to the 16th day (Figure S13 and Table S2). In addition, judging from the hematoxylin and eosin (H&E)-stained tumor tissue section collected in 2 h post treatment (Figure S14), unlike the tumors treated with POM or NIR alone, there are serious tissue damage and prominent cell apoptosis featuring karyopyknosis, karyorrhexis, and enormous formations of apoptotic bodies observed in the tumors with POM-mediated photothermal treatment. Taken together, these results suggest the outstanding anticancer efficiency of POM-mediated photothermal therapy, and their remarkable potential to serve as an excellent PA imaging agent.

2.5. Specificity of POM-Mediated Photothermal Therapy. Depending on the environmental redox level under different oxygen concentrations, the observations that the POM clusters exihibited a self-adaptive NIR absorbance (Figure S15) accordingly led us to further test their potential therapeutic specificity. After being co-incubated with POM for 12 h respectively in the normoxic (21% O_2) and hypoxic (2% O_2) atmosphere, the MCF-7 cells were then irradiated by 808 nm NIR laser for 5 min. Noticeably, the hypoxia-incubated POM clusters present a much enhanced photothermal conversion efficiency resulting in a 6 °C higher temperature rise than that incubated in the normoxic case (Figure 7a). Judging from the subsequent apoptosis assay of comparing the therapeutic efficiency between the two cases, there is a 1-fold increase in MCF-7 cells killing in the hypoxic case in comparison to that treated with normoxia-POM-mediated photothermal therapy (Figure 7b), suggesting POM a remarkable hypoxia-enhanced photothermal agent.

To evaluate the therapeutic specificity *in vivo*, the tri-4T1-tumors-bearing mice were irradiated with an expanded 808 nm laser beam to cover all three tumors including their surroundings in 1 h post i.v. injection of saline or POM (Figure 8a). In 5 min of irradiation, a relatively homogeneous temperature rise up to <40 °C can be observed in the irradiated region injected with saline (Figure 8b,d), which is too low to have a significant therapeutic effect. Excitingly, there is a much enhanced temperature contrast between the tumors and tissues

DOI: 10.1021/jacs.6b03375
J. Am. Chem. Soc. 2016, 138, 8156−8164

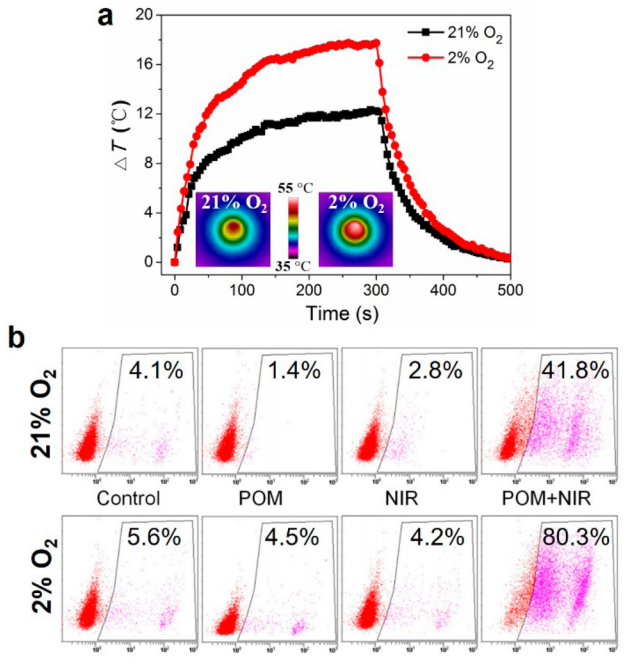

Figure 7. (a) Time-dependent temperature records of 808 nm laser irradiated POM-containing DMEMs after incubation in normoxic (21% O_2) and hypoxic (2% O_2) atmospheres for 12 h, indicating a hypoxic-enhanced photothermal conversion. Insets are the representative thermal images of the two cases. (b) Flow cytometry representing apoptosis assay based on propidium iodide-stained normoxic (first row) and hypoxic (second row) MCF-7 cells treated in different groups: control, POM incubation, 808 nm laser irradiation, and 808 nm laser irradiation after POM incubation.

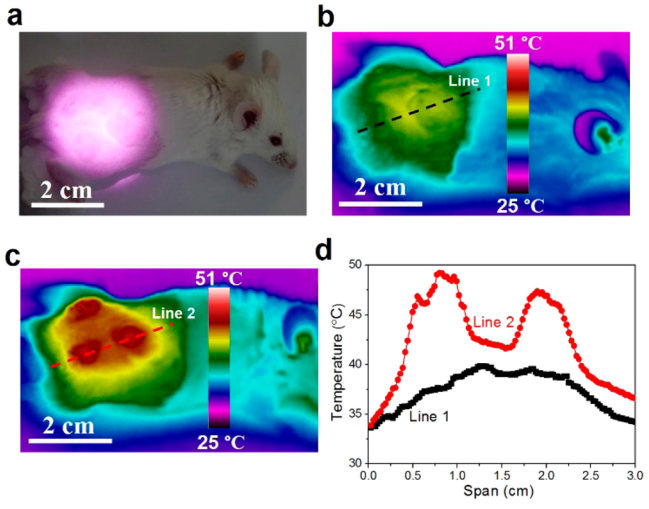

Figure 8. (a) Representative photograph of large-area 808 nm laser irradiation (1.5 W cm^{-2}, 5 min) on a tri-4T1-tumors-bearing Balb/c mouce. All three tumors surrounded by normal tissues nearby are covered by the 808 nm laser beam. Representative thermal images in 5 min expanded 808 nm laser irradiation (as shown in (c)) in 1 h post i.v. injection of saline (b) and POM (c, 30 mg Mo kg^{-1}). (d) Line distribution of temperatures in (b) (line 1) and (c) (line 2).

nearby in the POM-mediated photothermal therapy, where the tumor temperature reaches above 47 °C, with the normal tissues nearby remaining at <42 °C (Figure 8c,d), leading to efficient inhibitions on all tumors with no detectable damage upon nontumorous regions under the whole-area irradiation (Figures S16 and S17), which clearly indicates that POM could play a role as a highly tumor-selective photothermal agent.

Furthermore, to gain fundamental insight into the reveled POM-mediated tumor-specific photothermal therapy, we then performed detailed investigations on the potential differences of POM in the tumor tissue and the normal tissue nearby. Judging from the photoacoustic oxygenation map (Figure 9a), the tumor at this stage is revealed to be of much lower oxygen saturation than that of the normal tissue nearby, which confirms the well-known fact of a reductive microenvironment in the hypoxia tumor. Then, in 1 h after i.v. injection of POM, the tumor tissue, corresponding muscle tissue nearby, and skin tissue on the tumor were collected for XPS analysis to confirm the redox state of Mo in these tissues. As shown in Figure 9b, the observed S element is considered to come from tissue protein. In line with the LDIMS results (Figure 5d), negligible POM clusters can be detected in skin tissue. Importantly, the hypoxia tumor features not only higher POM accumulation than normal tissue, but also a higher proportion of Mo(V) in comparison to that in the muscle tissue nearby, evidently accounting for the higher photothermal conversion in such a more reductive tumor where more Mo(VI) in POM clusters has been reduced into Mo(V).

In contrast to the reducibility response, it is of significant difficulty to give a direct assessment on the acidity-induced self-assemble behavior of POM *in vivo*, but the above-revealed acidity-dependent absorption of POM provides an alternative strategy. We compared the total PA spectra of the tumor tissue to that of the muscle tissue nearby in 1 h post i.v. injection of POM. As shown in Figure 9c, the higher PA intensity of tumor tissue indicates a more efficient enrichment of POM in tumor than that in the muscle nearby. In addition, the characteristic absorption peak of POM at 860 nm in tumor approximates that of POM-dispersed solution of pH = 6.5 (Figure 3a), and shows a significant blue-shift in comparison to that in muscle tissue (881 nm). These interesting findings provide an available methodology to assess the tissular acidity using the as-prepared POM agent through PA imaging. Furthermore, numerous Mo-containing nanoaggregates have been detected in the tumor tissue (Figure 9d,f), which demonstrates the self-assembly behavior of POM in the tumor tissues. More interestingly, we found a further enhanced level of POM aggregate in the lysosome with pH = 4.5–5.0 (Figure 9e),[41] which is in line with the aforementioned *in vitro* results in aqueous solution (Figure 1). According to the above-demonstrated evidence that a lower pH value of 6.5 could lead to a significant self-assembly among POM clusters, and consequently a successive blue-shift of their absorption peak, this observed hypsochromic effect *in vivo* suggests an efficient aggregation of POM in the mildly acidic tumor microenvironment, which results in much more significant POMs' selective retention in tumor due to its much enlarged size. All these results confirms POM a smart acidity- and reducibility-specific photothermal agent *in vivo*, whose therapeutic efficiency could be activated and/or much enhanced through self-adaptive absorption change and self-assembly aggregation in the tumor microenvironment (Figure 9g).

3. CONCLUSIONS

Distinct from the well-researched nano-sized agents, we have successfully demonstrated a Mo-based polyoxometalate cluster paradigm for tumor-specific photothermal therapy, based on a unique naked electronic structure that is sensitive to its

DOI: 10.1021/jacs.6b03375
J. Am. Chem. Soc. 2016, 138, 8156–8164

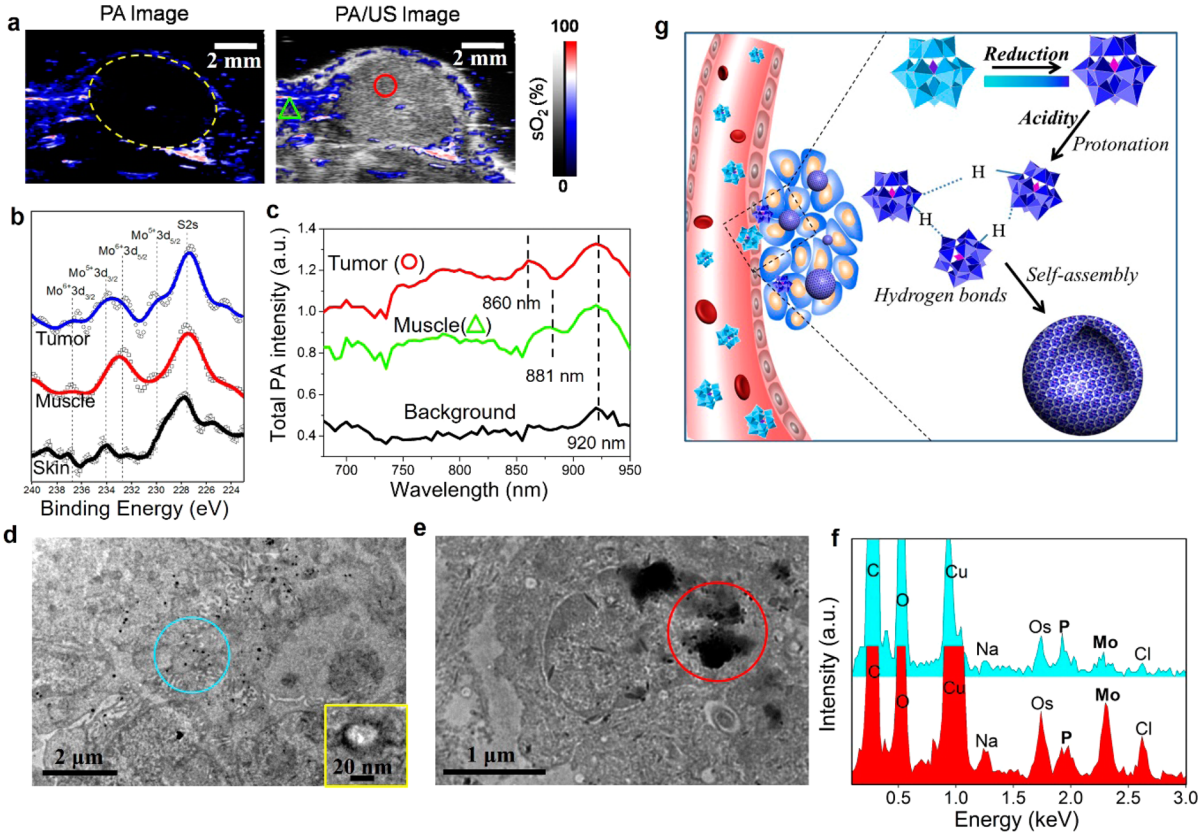

Figure 9. (a) Photoacoustic oxygenation map co-registered with a high-resolution ultrasound image of a subcutaneous 4T1 tumor. (b) XPS spectra of Mo 3d in the tumor tissue, muscle tissue (near the tumor), and skin tissue on the tumor collected in 1 h after i.v. injection of POM. (c) *In vivo* PA spectroscopic signals of tumor tissue (○) and muscle tissue (△) nearby measured in 1 h post i.v. injection of POM (30 mg Mo kg^{-1}). TEM images of wide-view tumor tissue (d) and a lysosome (e). Inset in (d) highlights the characteristic vesicle-like morphology of a self-assembled POM nanoparticle in acidic tumor. (f) EDS element analysis of the corresponding marked regions in (d) and (e), respectively. (g) Schematic diagram of the self-adaptive behavior of POM in response to the intratumoral acidity and reducibility *in vivo*.

microenvironment. Such a cluster shows a smart dual-response to both the acidity and reducibility in the tumor microenvironment, resulting in cluster assembly into much larger nanosizes for enhanced intratumoral accumulation and electron structural change for self-adaptive photothermal conversion. In addition to providing an especially promising clinical photothermal agent, this finding is expected to establish a new physicochemical paradigm for smart theranostic medicine design based on clusters, breaking through the conventional concepts of "molecule" or "nano" in biomedicine. Ongoing efforts are focused on screening the abundant POM family to further identify more promising theranostic candidates for clinical translation.

4. EXPERIMENTAL SECTION

4.1. Chemicals. Hexaammonium molybdate tetrahydrate ($(NH_4)_6Mo_7O_{24}\cdot 4H_2O$), sodium dihydrogen phosphate dodecahydrate ($NaH_2PO_4\cdot 12H_2O$), and L-ascorbic acid were purchased from Sinopharm Chemical Reagent Co., Ltd., China. All chemical agents are of analytical grade and were used directly with no further purification. Ultrapure water used throughout the experiments was prepared using an ELGA water purification system (PURELAB Classic).

4.2. Preparation of POM Clusters at Different Reduction States. The keggin-type POM was synthesized by a facile one-pot approach. First, 5 mmol $(NH_4)_6Mo_7O_{24}\cdot 4H_2O$ was dissolved in 10 mL of ultrapure water with a continuous stirring at 25 °C. A 5 mL solution of 2.92 mmol of $NaH_2PO_4\cdot 12H_2O$ was then rapidly added into the system. Subsequently, to obtain the reduced POM with different reduction state, another 2 mL solution of L-ascorbic acid at various concentrations of 150, 375, 900, and 1500 mg mL^{-1} was respectively added dropwise into the system under stirring. The obtained samples at different degree of reduction were correspondingly labeled as *R*1, *R*2, *R*3, and *R*4 in comparison to *Ox*, which is the oxidation state with no addition of L-ascorbic acid. After further stirring at 25 °C for 15 min, the resulting clusters were precipitated by addition of 80 mL of ethanol, collected by centrifugation, washed with water and ethanol for three times, and finally dried in a lyophilizer to obtain cluster powders.

4.3. Material Characterization. TEM images were acquired with JEM-2100F transmission electron microscope at 200 kV. The size distribution and zeta potential were measured by dynamic light scattering using a Malvern Zetesizer (Nano-ZS90) instrument. The quantitative analysis of element content in nanoparticles was performed with Agilent 700 Series inductively coupled plasma optical emission spectrometry (ICP-OES). UV−vis spectrum was recorded on a Shimadzu UV-3600 spectrophotometer. XPS measurement was performed on a Thermo Fisher Scientific ESCALab250 spectrometer. X-band EPR spectra were measured at room temperature in perpendicular mode on a Bruker EMX-8/2.7 spectrometer and recorded with the following settings: microwave frequency, 9.871 GHz; microwave power, 2.01 mW; modulation frequency, 100.00 kHz; and modulation amplitude, 4.00 G.

4.4. XAFS Data Collection. These POM clusters with different degree of reduction (*Ox*, *R*1, *R*2, *R*3, and *R*4) were respectively dissolved in 1 mL of water (50 mg Mo mL^{-1}) and stored in a 1.5 mL eppendorf tube for XAS measurement. The POM-*R*4 solution at pH = 7.4, 6.5, and 4.5 was adjusted through the addition of NaOH and HCl. The X-ray absorption data at the Mo K-edge (19.999 keV) of the samples were recorded at room temperature in transmission mode using ion chambers with silicon drift fluorescence detector at beamline

DOI: 10.1021/jacs.6b03375
J. Am. Chem. Soc. 2016, 138, 8156−8164

BL14W1 of the Shanghai Synchrotron Radiation Facility, China. The station was operated with a Si (311) double crystal monochromator. During the measurement, the synchrotron was operated at an energy of 3.5 GeV and a current between 150 and 210 mA. The photon energy was calibrated with the first inflection point of Mo K-edge in Mo metal foil. XAFS data reduction and analysis were performed using the software Athena.

4.5. Inhibitory Effect in Cancer Cell Proliferation. MCF-7 cells were seeded (1×10^4 cells in 100 μL of DMEM per well) in sextuplicate in 96-well microplates, and allowed to adhere overnight. Then, the culture medium was replaced by 100 μL of fresh medium containing POM at various concentrations of 12, 25, 50, and 100 μg Mo mL^{-1}. Without any further co-incubation, these cells were irradiated by the 808 nm NIR cells for 5 min with different power densities of 0.7, 1.5, and 2.0 W cm^{-2}. Subsequently, the culture media were replaced by FBS-free medium containing 0.6 mg mL^{-1} 3-[4,5-dimethylthiazol-2-yl-]-2,5 -diphenyltetrazolium bromide (MTT) and co-incubated for 4 h. The MTT solution was then replaced by 100 μL of dimethyl sulfoxide to solubilize the formazan. Cell proliferation was determined by monitoring the absorbance at λ = 490 nm using a microplate reader (Bio-TekELx800, USA) and expressed as the percentage of untreated control cells.

4.6. Anticancer Effect in 4T1-Tumor-Xenografted Mice. All animal experiments operations were performed in accordance with the protocols approved by Institutional Animal Care and Use Committee (IACUC) and the care regulations approved by the administrative committee of laboratory animals of Fudan University. Six 4T1-tumor-bearing mice per group were randomly allocated for different treatments. First, 100 μL of saline without or with POM (30 mg Mo kg^{-1}) was injected through a tail vein. At 1 h post injection, mice were anesthetized with 80 μL of 10 wt % chloral hydrate, and tumors were irradiated for 5 min by using an 808 nm laser with an 8 mm spot size at a power density of 1.5 W cm^{-1}. The tissue temperatures were recorded with an infrared camera. The maximum tumor length (L) and maximum tumor width (W) were measured every other day with a digital caliper, and the tumor volume (V) was calculated as $V = LW^2/2$. The relative tumor volume (V) was normalized to their initial volume (V_0). At 2 h post treatment, the pathological tissue sections of tumors were obtained from a random one among each group for H&E staining assay. When the tumor volume reached 1000 mm^3 at 16 days post treatment, the mice were euthanized and dissected to count the individuals with metastatic nodules in the lung for each group.

4.7. *In Vivo* Specificity of Photothermal Therapy. Tri-4T1-tumors-bearing mice were used to estimate the specificity of photothermal therapy *in vivo*. During the irradiation with an expended 808 nm laser (1.5 W cm^{-2}) to cover all tumors in 1 h post i.v. injection of saline or POM (30 mg Mo kg^{-1}) for 5 min, the tissue temperatures were recorded with an infrared camera. In the meantime, the mice in 1 h post injection of POM were euthanized to collect the skin tissue on the tumor, tumor tissue, and muscle tissue nearby. These collected tissues were frozen by immersion in liquid nitrogen and dried under vacuum for XPS measurements to analyze the reduction state of Mo. The relative tumor volumes were recorded every other day for 16 days with the i.v. injection of saline as control (three Tri-4T1-tumors bearing mice for each group). The tumor tissue was collected in 1 h post i.v. injection of POM (30 mg Mo kg^{-1}), fixed with 2.5% glutaraldehyde and 1% osmic acid, dehydrated, and then sliced into ultrathin sections for Bio-TEM (JEM-1400$^+$) analysis.

4.8. Statistical Analysis. Quantitative data were expressed as mean ± s.d. Statistical comparisons were conducted by using Student's two-tailed t test. A value of $P < 0.05$ was considered statistically significant.

■ ASSOCIATED CONTENT

Supporting Information

The Supporting Information is available free of charge on the ACS Publications website at DOI: 10.1021/jacs.6b03375.

Full methods, additional experimental data, and discussion, including Figures S1−S17 and Tables S1 and S2 (PDF)

■ AUTHOR INFORMATION

Corresponding Authors

*wbbu@mail.sic.ac.cn

*jlshi@mail.sic.ac.cn

Notes

The authors declare no competing financial interest.

■ ACKNOWLEDGMENTS

This work was financially supported by the National Natural Science Foundation of China (Grant Nos. 51372260, 51132009, and 81471714). The authors thank beamline BL14W1 (Shanghai Synchrotron Radiation Facility) for providing the beam time, and Heliang Yao and Jingwei Feng from Shanghai Institute of Ceramics, Chinese Academy of Sciences, for useful discussions.

■ REFERENCES

(1) Bogaerts, W. F.; Lampert, C. M. *J. Mater. Sci.* **1983**, *18*, 2847.
(2) Linic, S.; Christopher, P.; Ingram, D. B. *Nat. Mater.* **2011**, *10*, 911.
(3) Liu, G. L.; Kim, J.; Lu, Y.; Lee, L. P. *Nat. Mater.* **2006**, *5*, 27.
(4) Cheng, L.; Wang, C.; Feng, L.; Yang, K.; Liu, Z. *Chem. Rev.* **2014**, *114*, 10869.
(5) Jin, C. S.; Lovell, J. F.; Chen, J.; Zheng, G. *ACS Nano* **2013**, *7*, 2541.
(6) Fuchs, J.; Thiele, J. *Free Radical Biol. Med.* **1998**, *24*, 835.
(7) Huang, X.; Tang, S.; Mu, X.; Dai, Y.; Chen, G.; Zhou, Z.; Ruan, F.; Yang, Z.; Zheng, N. *Nat. Nanotechnol.* **2011**, *6*, 28.
(8) Au, L.; Zheng, D.; Zhou, F.; Li, Z.-Y.; Li, X.; Xia, Y. *ACS Nano* **2008**, *2*, 1645.
(9) Zhou, M.; Zhang, R.; Huang, M.; Lu, W.; Song, S.; Melancon, M. P.; Tian, M.; Liang, D.; Li, C. *J. Am. Chem. Soc.* **2010**, *132*, 15351.
(10) Chou, S. S.; Kaehr, B.; Kim, J.; Foley, B. M.; De, M.; Hopkins, P. E.; Huang, J.; Brinker, C. J.; Dravid, V. P. *Angew. Chem.* **2013**, *125*, 4254.
(11) Hessel, C. M.; Pattani, V. P.; Rasch, M.; Panthani, M. G.; Koo, B.; Tunnell, J. W.; Korgel, B. A. *Nano Lett.* **2011**, *11*, 2560.
(12) Chen, Z.; Wang, Q.; Wang, H.; Zhang, L.; Song, G.; Song, L.; Hu, J.; Wang, H.; Liu, J.; Zhu, M. *Adv. Mater.* **2013**, *25*, 2095.
(13) Poland, C. A.; Duffin, R.; Kinloch, I.; Maynard, A.; Wallace, W. A.; Seaton, A.; Stone, V.; Brown, S.; MacNee, W.; Donaldson, K. *Nat. Nanotechnol.* **2008**, *3*, 423.
(14) Liu, Z.; Davis, C.; Cai, W.; He, L.; Chen, X.; Dai, H. *Proc. Natl. Acad. Sci. U. S. A.* **2008**, *105*, 1410.
(15) Li, M.; Yang, X.; Ren, J.; Qu, K.; Qu, X. *Adv. Mater.* **2012**, *24*, 1722.
(16) Robinson, J. T.; Tabakman, S. M.; Liang, Y.; Wang, H.; Sanchez Casalongue, H.; Vinh, D.; Dai, H. *J. Am. Chem. Soc.* **2011**, *133*, 6825.
(17) Lovell, J. F.; Jin, C. S.; Huynh, E.; Jin, H.; Kim, C.; Rubinstein, J. L.; Chan, W. C.; Cao, W.; Wang, L. V.; Zheng, G. *Nat. Mater.* **2011**, *10*, 324.
(18) Cheng, L.; Yang, K.; Chen, Q.; Liu, Z. *ACS Nano* **2012**, *6*, 5605.
(19) Zheng, M.; Yue, C.; Ma, Y.; Gong, P.; Zhao, P.; Zheng, C.; Sheng, Z.; Zhang, P.; Wang, Z.; Cai, L. *ACS Nano* **2013**, *7*, 2056.
(20) Liu, Y.; Ai, K.; Liu, J.; Deng, M.; He, Y.; Lu, L. *Adv. Mater.* **2013**, *25*, 1353.
(21) Peer, D.; Karp, J. M.; Hong, S.; Farokhzad, O. C.; Margalit, R.; Langer, R. *Nat. Nanotechnol.* **2007**, *2*, 751.
(22) Juillerat-Jeanneret, L. *Drug Discovery Today* **2008**, *13*, 1099.
(23) Ferrari, M. *Nat. Rev. Cancer* **2005**, *5*, 161.
(24) Albanese, A.; Tang, P. S.; Chan, W. C. *Annu. Rev. Biomed. Eng.* **2012**, *14*, 1.

DOI: 10.1021/jacs.6b03375
J. Am. Chem. Soc. 2016, 138, 8156−8164

(25) Nel, A. E.; Mädler, L.; Velegol, D.; Xia, T.; Hoek, E. M.; Somasundaran, P.; Klaessig, F.; Castranova, V.; Thompson, M. *Nat. Mater.* **2009**, *8*, 543.
(26) Huynh, E.; Leung, B. Y.; Helfield, B. L.; Shakiba, M.; Gandier, J.-A.; Jin, C. S.; Master, E. R.; Wilson, B. C.; Goertz, D. E.; Zheng, G. *Nat. Nanotechnol.* **2015**, *10*, 325.
(27) Wang, L.; Yang, P.-P.; Zhao, X.-X.; Wang, H. *Nanoscale* **2016**, *8*, 2488.
(28) Pu, K.; Shuhendler, A. J.; Jokerst, J. V.; Mei, J.; Gambhir, S. S.; Bao, Z.; Rao, J. *Nat. Nanotechnol.* **2014**, *9*, 233.
(29) Weissleder, R. *Nat. Biotechnol.* **2001**, *19*, 316.
(30) Danhier, F.; Feron, O.; Préat, V. *J. Controlled Release* **2010**, *148*, 135.
(31) Li, H.; Fan, X.; Houghton, J. *J. Cell. Biochem.* **2007**, *101*, 805.
(32) Liu, T.; Diemann, E.; Li, H.; Dress, A. W.; Müller, A. *Nature* **2003**, *426*, 59.
(33) Liu, T.; Langston, M. L.; Li, D.; Pigga, J. M.; Pichon, C.; Todea, A. M.; Müller, A. *Science* **2011**, *331*, 1590.
(34) Ganapathy, S.; Fournier, M.; Paul, J.; Delevoye, L.; Guelton, M.; Amoureux, J. *J. Am. Chem. Soc.* **2002**, *124*, 7821.
(35) Taketa, H.; Katsuki, S.; Eguchi, K.; Seiyama, T.; Yamazoe, N. *J. Phys. Chem.* **1986**, *90*, 2959.
(36) Lopez, X.; Maestre, J. M.; Bo, C.; Poblet, J.-M. *J. Am. Chem. Soc.* **2001**, *123*, 9571.
(37) Buckley, R. I.; Clark, R. J. *Coord. Chem. Rev.* **1985**, *65*, 167.
(38) Choi, H. S.; Liu, W.; Misra, P.; Tanaka, E.; Zimmer, J. P.; Itty Ipe, B.; Bawendi, M. G.; Frangioni, J. V. *Nat. Biotechnol.* **2007**, *25*, 1165.
(39) Heldin, C.-H.; Rubin, K.; Pietras, K.; Östman, A. *Nat. Rev. Cancer* **2004**, *4*, 806.
(40) Holback, H.; Yeo, Y. *Pharm. Res.* **2011**, *28*, 1819.
(41) Schmaljohann, D. *Adv. Drug Delivery Rev.* **2006**, *58*, 1655.

DOI: 10.1021/jacs.6b03375
J. Am. Chem. Soc. 2016, 138, 8156−8164